

Numerical analysis of deformations in deep twin tunnels with a transverse gallery

Bianca M. Girardi¹, Felipe P. M. Quevedo¹, Samir Maghous¹

¹*Graduate Program in Civil Engineering, Federal University of Rio Grande do Sul
Av. Osvaldo Aranha, 99, Porto Alegre, 90.035-190, RS, Brazil
eng.biancagirardi@gmail.com, motta.quevedo@ufrgs.br, samir.maghous@ufrgs.br*

Abstract. The increasing construction of twin tunnels demands a comprehensive understanding of their interaction with transverse galleries and the surrounding rock mass. This study conducts a 3D finite element analysis of the junction between deep twin tunnels and a transverse gallery, incorporating time-dependent effects such as rock mass creep, concrete creep, and shrinkage. The model is verified against existing numerical results, confirming its reliability in estimating internal forces in the lining. A comparison of different rock mass friction angles demonstrates their impact on deformation and pressure distributions along the lining, providing relevant insights for design and reinforcement strategies. The results indicate pronounced anisotropy in both deformations and pressures, influenced by the properties of the lining and the rock mass. Maximum deformations occur at the crown, reflecting a tendency of horizontal ovalization, while minimum displacements and peak pressures are observed at the lateral sides of the walls. Higher friction angles reduce both convergence and pressure, particularly at the end of construction. Viscoelastic linings show increased long-term redistribution of stresses and deformations. The study reinforces the importance of 3D modeling and time-dependent behavior in the safe and accurate design of tunnel-gallery intersections.

Keywords: Deep twin tunnels, Transverse gallery, Viscoelastic concrete lining, Elastoplastic-viscoplastic coupled, Finite element model

1 Introduction

The increasing demand for underground infrastructure in urban areas has led to a rise in the construction of twin tunnels, typically designed for one-way traffic in each tunnel. For operational and safety purposes, transverse galleries are often incorporated, allowing for interconnections between tunnels. These junction zones represent critical areas in tunnel design due to the complex interactions between the tunnel linings, surrounding rock mass, and construction sequence.

Despite advances in tunneling technology, the interaction mechanisms induced by transverse galleries, especially in deep tunneling scenarios, remain underexplored, mainly due to the computational complexity involved in modeling 3D geometries and sequential excavation processes. The excavation of a transverse gallery causes a redistribution of stresses in the surrounding rock mass, resulting in increased loads on the main tunnel lining near the intersection. When these additional loads exceed the structural capacity of the primary lining, localized instability may occur, raising the risk of failure. Therefore, understanding how deformations and pressures are redistributed in this zone is crucial for the proper design of linings and the placement of structural reinforcements. Incorporating these effects into the design process is essential to ensure the structural integrity and long-term stability of the tunnel system.

The present work extends a previous numerical study by Quevedo et al. [1], providing a detailed three-dimensional finite element analysis of deep twin tunnels connected by a transverse gallery. A coupled elastoplastic-viscoplastic constitutive model is used for the rock mass, while the concrete lining behavior includes viscoelasticity and shrinkage effects. Special attention is given to the anisotropic redistribution of lining deformations and pressures in the junction zone, considering different friction angles in the rock mass and comparing elastic and viscoelastic linings.

The results aim to support design decisions by highlighting the importance of using advanced material models and 3D simulations in the analysis of tunnel-gallery intersections, particularly under long-term conditions.

2 Constitutive models

The structural response of the tunnel system is governed by time-dependent behaviors in both the concrete lining and the surrounding rock mass.

2.1 Concrete lining

The viscoelastic behavior of concrete is modeled using the Solidification Theory developed by Bažant and Prasannan [2, 3], calibrated with the CEB-FIP Model Code 1990 standard specifications formulation described in CEB-FIP [4]. This formulation enables the simulation of delayed deformations and stress redistribution caused by creep and shrinkage in the lining. The creep strain is represented through a Generalized Kelvin chain with aging, while shrinkage is introduced as an isotropic strain field.

The stress–strain relationship under small deformations is expressed as:

$$\Delta\sigma = \mathbf{D} : \Delta\epsilon - \mathbf{D} : \Delta\epsilon^{sh} - \mathbf{D}^* : \Delta\epsilon^{cr} \quad (1)$$

where \mathbf{D} is the elastic stiffness tensor, \mathbf{D}^* is the same tensor reformulated to account for the viscoelastic effects due to concrete aging, and $\Delta\epsilon^{sh}$ and $\Delta\epsilon^{cr}$ are the shrinkage and creep strain increments, respectively.

To match the CEB-FIP MC90 formulation, the parameters of the Bažant-Prasannan model are calibrated through the following equivalences:

$$E_0 = E_c(t_0), \quad \gamma(t - t_0) = \beta_c(t - t_0), \quad \frac{1}{v(t)} = \frac{\varphi_0(t_0)}{E_{ci}}, \quad \frac{1}{\eta(t)} \rightarrow 0 \quad (2)$$

In Equation (2), t_0 represents the concrete age at the time of loading; $E_c(t_0)$ is the tangent modulus at loading; $\beta_c(t - t_0)$ is a function of the duration under load; $\varphi_0(t_0)$ is the basic creep coefficient; E_{ci} is the elastic modulus at 28 days; and $\eta(t)$ is the apparent macroscopic viscosity, which tends to infinity, reflecting the solidification concept. This calibration allows for a realistic representation of the aging viscoelastic behavior using a constant set of coefficients.

2.2 Rock mass

The rock mass is modeled using a coupled elastoplastic-viscoplastic formulation under infinitesimal strain theory. The total strain rate ($\dot{\epsilon}$) is decomposed into elastic ($\dot{\epsilon}^e$), plastic ($\dot{\epsilon}^p$), and viscoplastic ($\dot{\epsilon}^{vp}$) components:

$$\dot{\epsilon} = \dot{\epsilon}^e + \dot{\epsilon}^p + \dot{\epsilon}^{vp} \quad (3)$$

The short-term behavior is captured using the Drucker–Prager yield criterion:

$$f^p(\sigma, q) = f^p(I_1, J_2, q^p) = \beta_1 I_1 + \beta_2 \sqrt{J_2} - q^p(\alpha^p) \quad (4)$$

The yield surface is defined in terms of the first invariant of stress tensor I_1 , the second invariant of the deviator tensor J_2 , the parameter related to cohesion $q^p(\alpha^p)$ and the strength parameters related to the friction angle β_1 and β_2 . These terms are given by:

$$\beta_1 = \frac{(k^p - 1)}{3}, \beta_2 = \frac{(2k^p + 1)}{\sqrt{3}}, q^p(\alpha^p) = 2\sqrt{k^p} c^p(\alpha^p) \quad (5)$$

where $k^p = (1 + \sin \phi^p)/(1 - \sin \phi^p)$ and α^p is the internal variable associated with the hardening and softening of the material.

The viscosity parameter and power-law exponent govern the rate of viscoplastic deformation. This formulation allows for the simulation of both instantaneous and time-dependent effects relevant to the deep tunnel environment.

Consistent with the elastoplastic approach, the viscoplastic yield function also adopts the Drucker–Prager yield criterion. As a consequence, the coefficients β_1 and β_2 of eq. (5) are evaluated by replacing k^p for $k^{vp} = (1 + \sin \phi^{vp}) / (1 - \sin \phi^{vp})$. Also, the viscoplastic cohesion parameter then becomes $q^{vp} = 2\sqrt{k^{vp}c^{vp}(\alpha^{vp})}$. In this study, both plastic and viscous flow rules are implemented with associative potentials, assuming perfect plasticity and viscoplasticity (i. e., cohesions c^p and c^{vp} assumed to remain constant).

The plastic flow rule, governing the evolution of plastic deformations, is defined as:

$$\dot{\epsilon}^p = \begin{cases} \dot{\lambda}^p \frac{\partial g^p}{\partial \sigma}, & \text{for } f^p > 0, \\ 0, & \text{for } f^p \leq 0, \end{cases} \quad (6)$$

where $\dot{\lambda}^p$ denotes the plastic multiplier and g^p is the plastic potential function, analogous to the yield function f^p . The viscoplastic flow rule in eq. (6) is expressed by:

$$\dot{\epsilon}^{vp} = \dot{\lambda}^{vp} \frac{\partial f^{vp}}{\partial \sigma} \quad (7)$$

The viscoplastic multiplier $\dot{\lambda}^{vp}$ in equation above is given explicitly by the following expression:

$$\dot{\lambda}^{vp} = \frac{\Phi(\sigma, q^{vp})}{\eta} \quad (8)$$

where η is the dynamic viscosity constant (in MPa.day), $\Phi = \langle f^{vp}(\sigma, q^{vp}) \rangle^n$ is the overstress function, n is the dimensionless parameter controlling the power-law shape and $\langle * \rangle$ is the McCauley function, which results in zero when $* < 0$ ensuring that viscoplastic flow occurs only for positive overstress values.

3 Spatial and time discretization of the domain

The finite element simulations were performed using a three-dimensional model representing deep twin tunnels connected by a transverse gallery. The geometry was reduced by symmetry, modeling only one-quarter of the domain, represented as Ω (see Fig. 1). The analysis assumes deep tunnel conditions ($H \gg R_t$), with H being the overburden depth and R_t the longitudinal tunnel radius. The transverse gallery radius R_g is smaller than R_t ($R_g < R_t$).

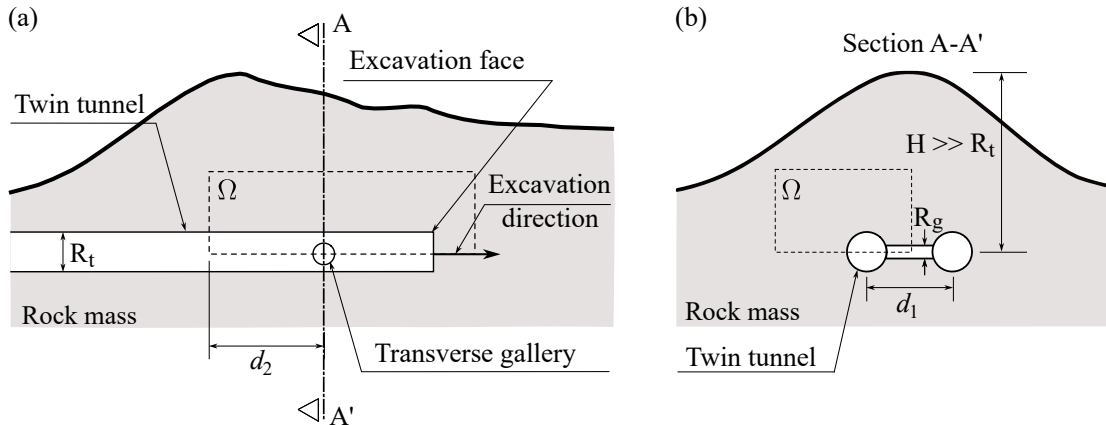


Figure 1. Schematic representation of the twin tunnels geometry problem: (a) longitudinal view and (b) section A-A'.

The computational domain consists of a parallelepiped volume with dimensions $(L_1 + L_2) \times L_3 \times d_3$, as presented in Fig. 2. Symmetry conditions are imposed on the planes $x = 0$, $y = 0$, and $z = L_1 + L_2$, reducing the computational cost of the analysis. This approach assumes that the longitudinal tunnels are excavated synchronously and the transverse gallery is excavated from the tunnels towards the center. Initial isotropic in-situ stresses are applied as boundary pressures: vertical stress σ_v at the upper plane and horizontal stress σ_h at the left-lateral and back planes.

Discretization is performed using 8-node trilinear hexahedral elements with full integration. In regions with complex geometry, such as the tunnel-gallery intersection, 8-node linear tetrahedral elements are used. A refined mesh is employed in the zones near the tunnel and gallery walls to ensure accuracy in stress and deformation fields. The total mesh consists of approximately 617,000 elements.

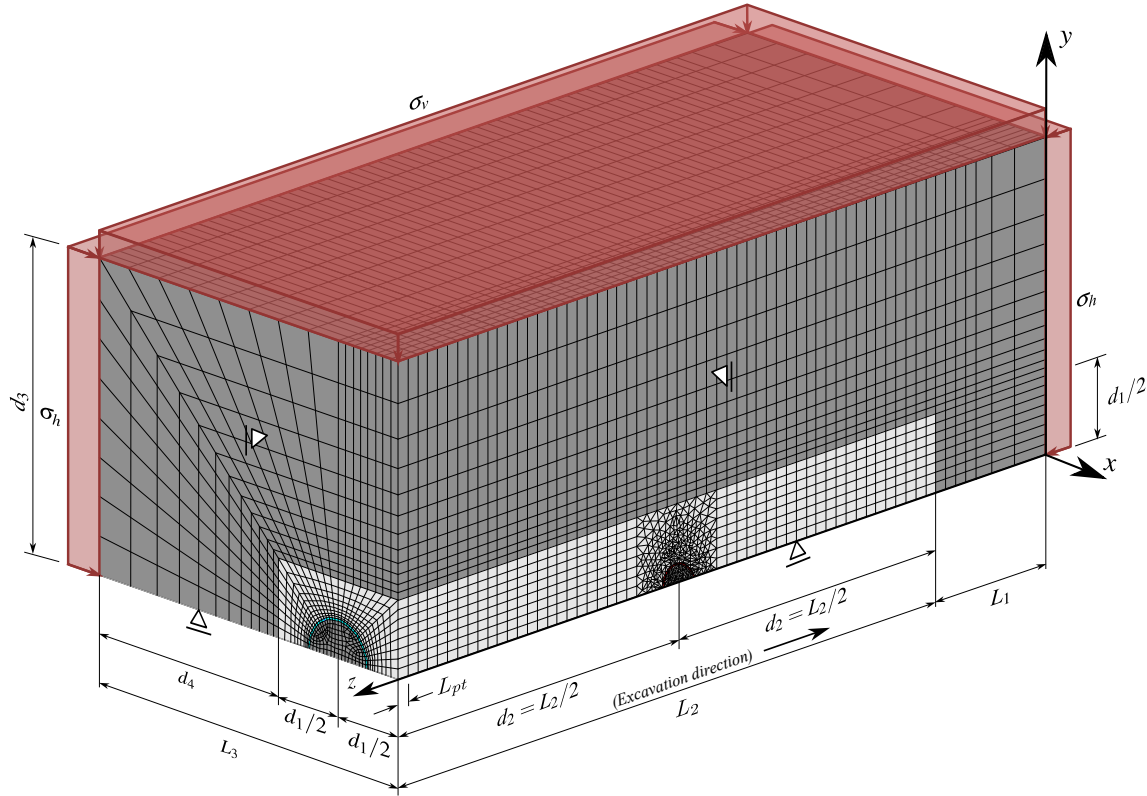


Figure 2. Mesh, dimensions and boundary conditions of the twin tunnels with gallery domain.

The excavation process is modeled using an activation–deactivation technique. The longitudinal tunnel excavation is simulated by deactivating solid elements (reducing their stiffness), followed by activation of lining elements after a specified distance from the face (d_{0t}). Each excavation step (L_{pt}) is associated with a time interval $t_p = L_{pt}/V_{pt}$, where $V_{pt} = 12.5$ m/day is the excavation speed. The gallery is excavated after complete a pre-defined number of steps (n_{pig}) in the longitudinal tunnel and follows the same procedure with L_{pg} , V_{pg} and d_{0g} . Table 1 presents the values adopted of the parameters related to the domain geometry, excavation and installation of the lining.

4 Verification

This section aims to verify the computational model's capability to simulate circumferential internal forces induced in the tunnel lining by the transverse gallery construction. For this verification, results from 3D finite element analyses by Chortis and Kavvadas [5] are compared with those obtained from the present F.E. model.

Chortis and Kavvadas [5] modeled the rock mass using solid elements and a linear elastic perfect plastic behavior based on the Generalized Hoek-Brown criterion. The shotcrete lining was represented by shell elements with linear elastic properties. In the present study, the Hoek-Brown criterion was approximated by the Mohr-

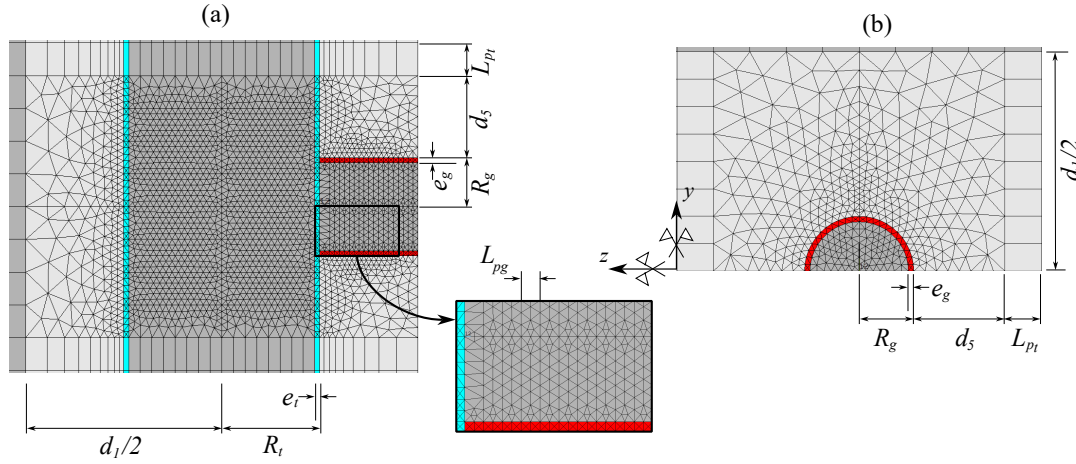


Figure 3. Geometry and F. E mesh: (a) longitudinal tunnel and gallery in the symmetry plane $y = 0$ and (b) gallery cross-section

Table 1. Geometric and construction parameters of the domain

Parameters	Symbol	Unit	Value
Longitudinal tunnels			
Radius	R_t	m	R_t
Thickness of the concrete lining	e_t	m	$0.05R_t$
Step length of the excavation process	L_{pt}	m	$R_t/3$
Unlined length	d_{0t}	m	$2R_t/3$
Gallery			
Radius	R_g	m	$0.5R_t$
Thickness of the concrete lining	e_g	m	$0.05R_t$
Step length of the excavation process	L_{pg}	m	$0.2R_g$
Unlined length	d_{0g}	m	0
Steps before gallery excavation	n_{pig}	un	15
Rest of domain			
Distance between longitudinal tunnel axes	d_1	m	$4R_t$
Thickness along vertical direction e_y	d_3	m	$20R_t$
Distance of transition zone between tetrahedral and hexahedral elements	d_5	m	$2L_p$
Length of the unexcavated region	L_1	m	$10R_t$
Total excavated length	L_2	m	$500L_{pt}$
Thickness along transversal direction e_z	L_3	m	$20R_t + d_1/2$

Coulomb model using the formulation proposed by Hoek et al. [6], obtaining yielding cohesion and friction angle values of 0.14 MPa and 28.72° , respectively, for implementation in the numerical model.

While Chortis and Kavvadas [5] explored a range of geometric and constitutive parameters through parametric analyses, in this study were adopted fixed values for these parameters: radius ratio between the longitudinal tunnel and the gallery $R_t/R_g = 1.33$, distance between longitudinal tunnel axes $d_1 = 8R_t$, overburden height $H = 80$ m, isotropic initial stress $\sigma_v = \sigma_h = 2$ MPa, rock mass Young modulus $E_m = 562$ MPa and Poisson ratio $\nu_m = 0.3$, shotcrete Young modulus $E_{c28} = 20$ GPa and Poisson ratio $\nu_c = 0.2$.

The internal forces in the tunnel lining were evaluated at the end of construction using a normalized circumferential $N_C^* = N_C/(p_0 D)$ component. In Figure 4 (a), results near the transverse gallery were consistent with those reported by Chortis and Kavvadas [5], confirming the concentration of effects in that region. Further from the gallery, lower values were observed, likely due to differences in modeling strategies, including element types,

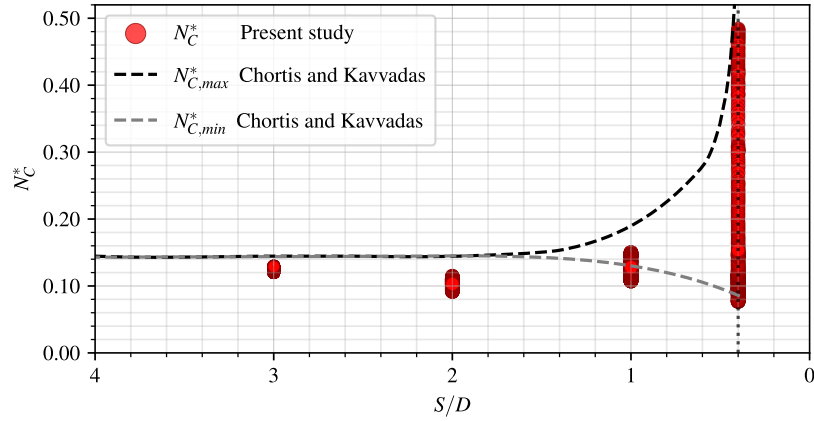


Figure 4. Normalized circumferential internal force on the main tunnel at the end of construction.

excavation procedures, and constitutive criteria.

5 Three-dimensional finite element simulations

This section presents numerical results related to the anisotropy of pressures and deformations in the twin tunnel walls, considering both elastic (EL) and viscoelastic (VEL) lining behaviors. The rock mass was modeled with an elastic modulus $E_m = 1400$ MPa and Poisson's ratio $\nu_m = 0.4$. The Drucker–Prager plasticity model was adopted with cohesion $c^p = 4$ MPa and friction angles $\phi^p = 0^\circ$ and 5° . Viscoplastic behavior was incorporated using a viscosity coefficient $\eta = 40,000$ MPa · day, viscoplastic cohesion $c^{vp} = 2$ MPa, and viscoplastic friction angle $\phi^{vp} = 0^\circ$. For the concrete lining, the 28-day elastic modulus was $E_{c28} = 25,146$ MPa and Poisson's ratio $\nu_c = 0.2$.

Numerical results of wall deformations and lining pressures are presented at the end of construction and after 3,000 days, representing long-term viscous stabilization. The anisotropies of deformations and pressures are represented, respectively, by:

$$\rho(\theta) = \frac{U(\theta)}{U(\theta = 90^\circ)} \text{ and } \chi(\theta) = \frac{p(\theta)}{p(\theta = 90^\circ)}, \quad (9)$$

where θ denotes the cylindrical angle along the tunnel wall perimeter, with convergence defined as $U(\theta) = -u_r(R_t, \theta)/R_t$ and $p(\theta)$ represents the pressure on the longitudinal tunnel lining. The values at $\theta = 90^\circ$, corresponding to the crown, are used as reference for comparison.

Two sections, S1 and S2, were adopted along the longitudinal tunnel and their locations are shown in Fig. 5. Section S2 is located at the centerline of the transverse gallery, while S1 is positioned at a distance of $4R_g/3$ along the z -axis. No results are available for $0^\circ < \theta < 30^\circ$ in S2, as this region corresponds to the gallery entrance.

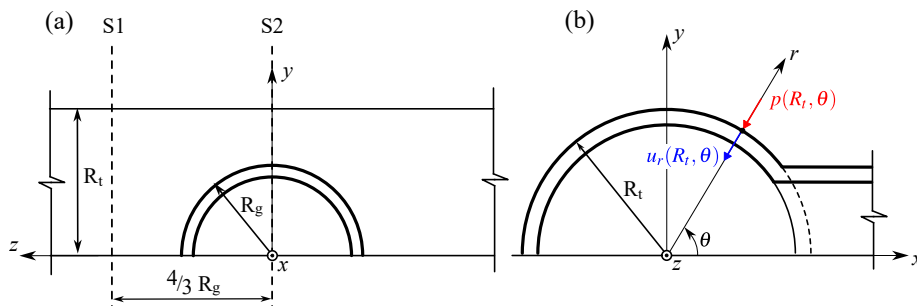


Figure 5. (a) Schematic representation of the sections S1 and S2 in the longitudinal tunnel, (b) S2 and representation of pressure and displacements on the lining.

In Fig. 6, the results show that tunnel deformations are greater at the crown ($\theta = 90^\circ$), with the lower

values at $\theta = 0^\circ < \theta < 30^\circ$, indicating a predominantly horizontal ovalization. Compared to the elastic model, viscoelastic linings show higher overall convergences, about 10% at the end of construction. In section S2, the lowest deformations occur near the gallery entrance, while for $\theta > 90^\circ$, the behavior becomes similar to the other section.

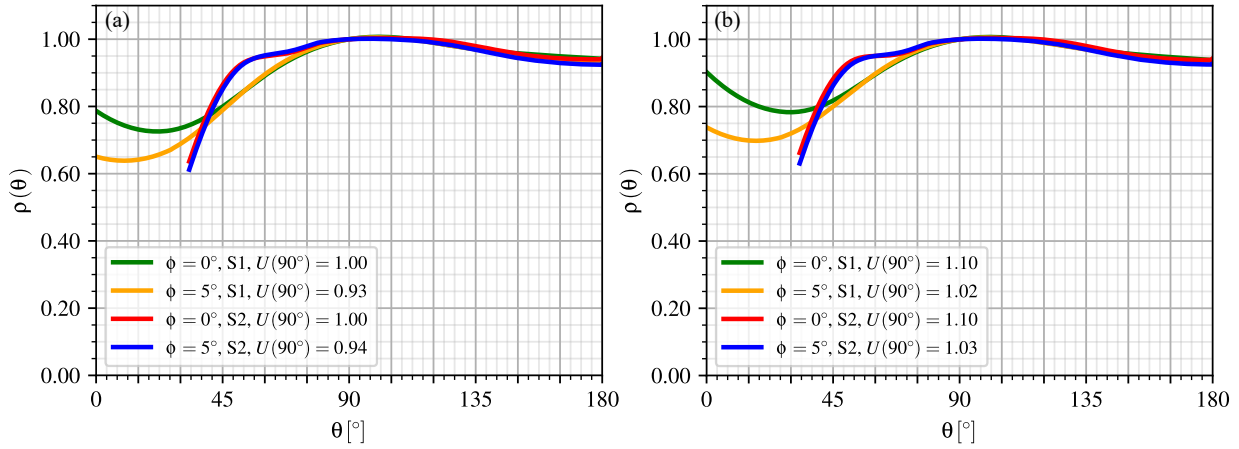


Figure 6. Anisotropy of deformations in longitudinal tunnel lining at the end of construction: (a) elastic lining (EL) and (b) viscoelastic lining (VEL).

The long-term behavior presented in Fig. 7 remains similar to that at the end of construction, with maximum deformations at the crown. Anisotropy decreases in the range $0^\circ \leq \theta \leq 45^\circ$, with the friction angle influencing not only the magnitude of deformations but also contributing to the anisotropic response. In section S2, despite higher convergences over time, the pattern between 30° and 75° remains consistent, suggesting minimal influence of the friction angle on anisotropy above the gallery entrance.

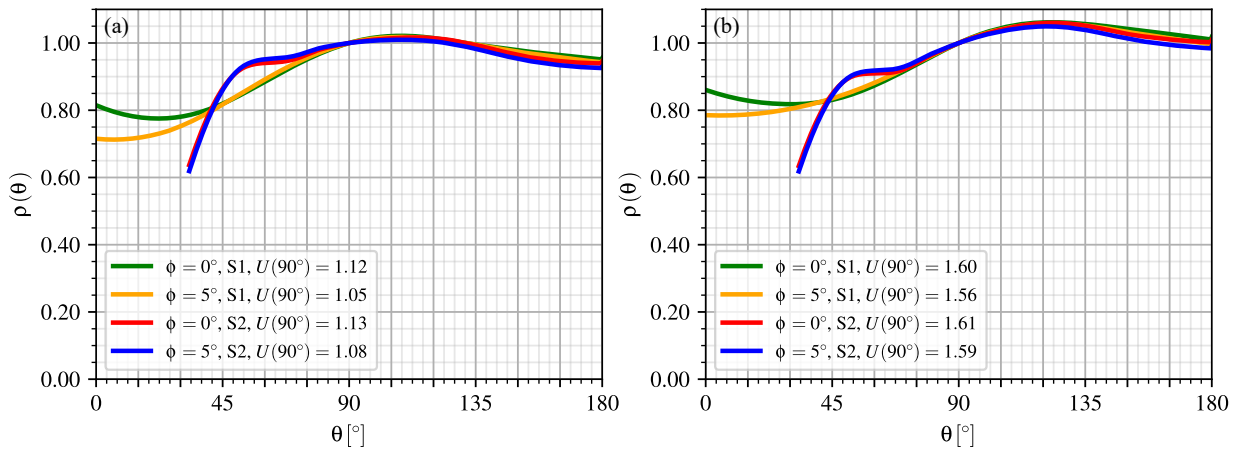


Figure 7. Anisotropy of deformations in longitudinal tunnel lining at long-term: (a) elastic lining (EL) and (b) viscoelastic lining (VEL).

Figure 8 shows that, at the end of construction, the lining pressures remain close to the reference value $p(\theta)$, except in the range $0^\circ < \theta < 60^\circ$, where a significantly increase is observed, reaching more than twice the crown pressure at $\theta = 0^\circ$. The friction angle influences pressure distribution, especially in section S2, where higher angles reduce pressures above the gallery entrance and amplify the contrast with the crown, reflecting greater rock mass support and lower stress transfer to the lining.

The long-term pressures presented in Fig. 9 have a similar behavior to the end of construction but with increased magnitudes, and the influence of the friction angle is less pronounced. Overall, stress concentrations tend

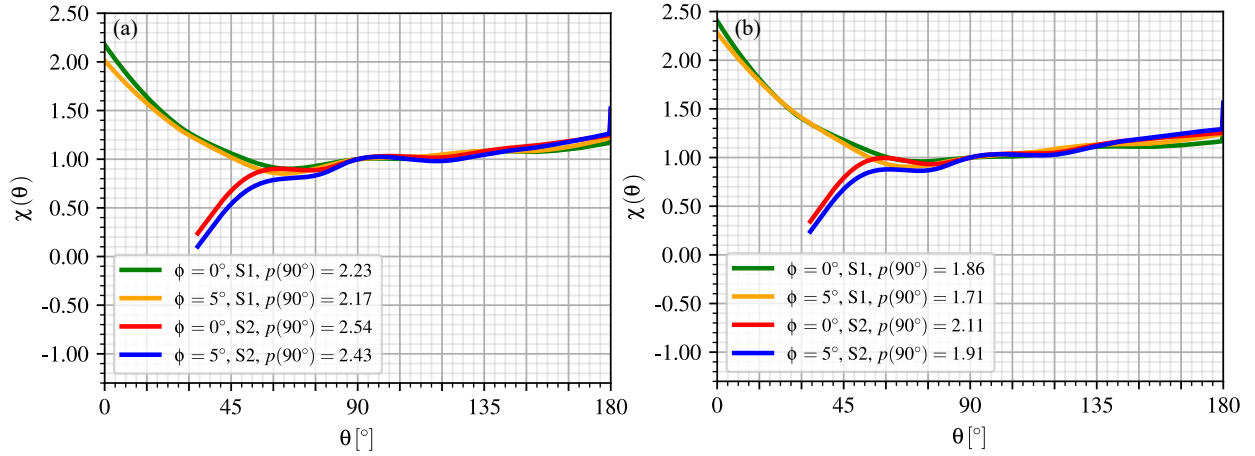


Figure 8. Anisotropy of pressures in longitudinal tunnel lining at the end of construction: (a) elastic lining (EL) and (b) viscoelastic lining (VEL).

to be higher at the lateral sides of the tunnels ($\theta = 0^\circ$ and 180°), indicating that regions with lower displacements are subjected to greater lining loads.

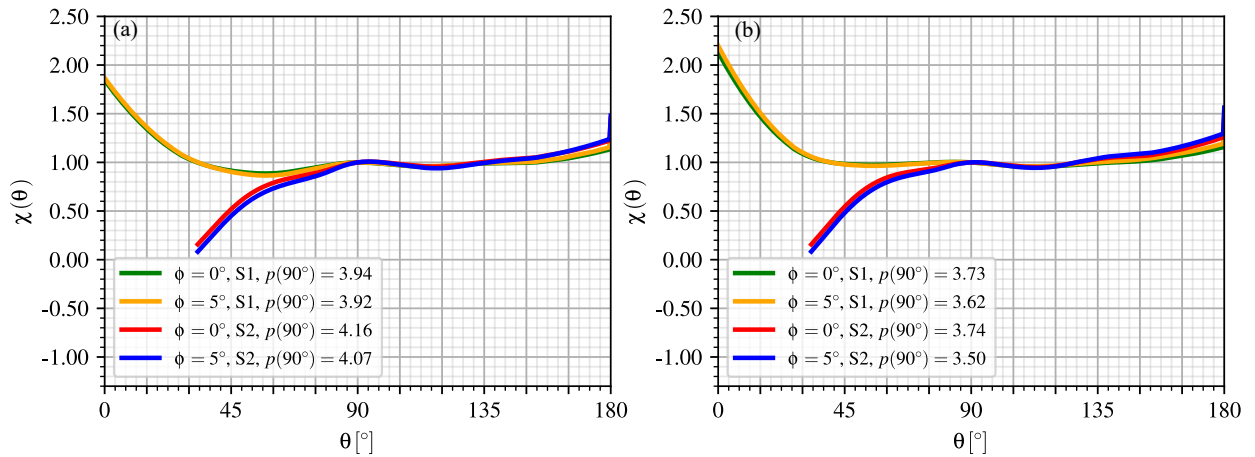


Figure 9. Anisotropy of pressures in longitudinal tunnel lining at long-term: (a) elastic lining (EL) and (b) viscoelastic lining (VEL).

6 Conclusions

The presence of a transverse gallery increases deformation and pressure anisotropy in adjacent tunnel linings, influenced by the lining behavior and rock mass friction angle. Viscoelastic linings show greater long-term convergence and stress redistribution, highlighting the importance of considering aging effects in tunnel design. The deformation analysis showed a consistent tendency of horizontal ovalization for both elastic and viscoelastic linings, with maximum deformations at the crown, except for a slight deviation in the long-term. The deformation anisotropy was only slightly influenced by the friction angle, which primarily affected the magnitude of deformations.

Pressure distribution showed higher values in areas of minimal convergence, especially between the twin tunnels. The rock mass friction angle had a stronger effect above the gallery entrance, where increased shear strength amplified anisotropy in the lining response.

Overall, the results highlight the importance of using advanced material models and 3D analyses for the

safe and realistic design of complex underground structures, especially in deep twin tunnel–gallery junctions with long-term and interactions conditions.

Acknowledgements. This section should be positioned immediately after the Conclusion section. Type Acknowledgements in boldface, 10 pt Times New Roman type from left margin, leaving 20 pt line spacing before and 12pt after.

Authorship statement. The authors hereby confirm that they are the sole liable persons responsible for the authorship of this work, and that all material that has been herein included as part of the present paper is either the property (and authorship) of the authors, or has the permission of the owners to be included here.

References

- [1] F. P. M. Quevedo, C. A. M. M. Colombo, D. Bernaud, and S. Maghous. 3d finite element analysis of rock deformation in twin circular tunnels with a transverse gallery using plasticity and time-dependent models. *Geotechnical and Geological Engineering*, vol. 1, n. 149, pp. 1–33, 202.
- [2] Z. P. Bažant and S. Prasannan. Solidification theory for concrete creep. I: Formulation. *Journal of Engineering Mechanics*, vol. 115, n. 8, pp. 1691–1703, 1989a.
- [3] Z. P. Bažant and S. Prasannan. Solidification theory for concrete creep. II: Verification and application. *Journal of Engineering Mechanics*, vol. 115, n. 8, pp. 1704–1725, 1989b.
- [4] CEB-FIP. *CEB-FIP model code 1990: Design code*. Comité Euro International du Béton and Fédération Internationale de la Précontrainte (CEB-FIP), 1993.
- [5] F. Chortis and M. Kavvadas. 3d numerical investigation of the axial forces acting on tunnel junctions constructed in fractured/weathered to very blocky rockmass. *Expanding Underground - Knowledge and Passion to Make a Positive Impact on the World*, pp. 1574–1582, 2023.
- [6] E. Hoek, C. Carranza-Torres, and B. Corkum. Hoek-brown failure criterion 2002 edition. *Proceedings of the North American Rock Mechanics Society Meeting*, pp. 267–273, 2002.